NUMERICAL SIMULATIONS BY GODUNOV-TYPE SCHEMES OF AIR-POLLUTANTS DYNAMICS

KRIS MURAWSKI AND JERZY K. MICHALCZYK

Institute of Environment Protection Engineering,
Department of Environmental Physics,
Technical University of Lublin,
Nadbystrzycka 40, 20-618 Lublin, Poland
kamur@akropolis.pol.lublin.pl,
jerzyk@akropolis.pol.lublin.pl

Abstract: In this paper several aspects associated with numerical simulations of hyperbolic equations are discussed. This presentation covers a range of modern shock-capturing schemes which are based on Godunov-type techniques. These schemes are well suited for strong shocks and other discontinuities, without generating spurious oscillations in the flow variables. An example of a performance of such schemes is provided to simulate the spatial distribution of air-pollutants which are emitted from a chimney. The simulations are performed in the framework of two-dimensional hydrodynamics, with a use of the CLAWPACK code [1]. The model reproduces several features of the distribution, including occurrence of vortices and plumes above the chimney.

Keywords: numerical discretization, hydrodynamic equations, distribution of air-pollutants

1. Premises of interest in numerical simulations

Traditionally the scientific methods involve a mutual interplay between experiments and analysis. The former try to collect information by repeated events. The latter attempts to order the accumulated knowledge. Analysis and experiment interact with each other via mutual stimulation and feedback. However, the traditional methods of investigating the nature have their limitations. Often a complexity of phenomena and a simultaneous interaction of various effects make a complete analysis impossible. On the experimental side, one is limited to measurements of only a small fraction of the quantities of interest and even they can be sampled only at a few times and spatial locations and with a limited degree of accuracy. Consequently, one is then faced with the task of interpreting limited observations with theories that are incomplete. For example for air-pollutants, due to a high cost of monitoring the available experimental data is often scarce and sporadic. Additionally, this data very often depends on time and space. The sheer volume of exploration in space

can be so large that the essential point measurements alone often lead to misinterpretation of the data.

Computer simulations – that is, the use of computers to solve problems by simulating theoretical models – are part of a new methodology that has taken its place alongside pure theory and experiment during the last 60 years or so. The basic idea of computer experiments is to simulate the behavior of natural systems by developing and solving a mathematical model, *i.e.* an appropriate set of mathematical equations, perhaps in the form of a set of differential equations, that are built on the basis of a physical model and that describe a particular physical system. Such equations are transformed to a discrete form and can be then numerically treated.

The feedback of numerical results into theoretical modeling and the continuous interaction with laboratory experiments and analytical theory make computing an indispensable tool for science. Numerical computations share characteristics with both analytical theories and laboratory experiments. Like analytical theories, numerical computations are based on theoretical concepts and attempt to predict the behavior of physical systems using abstract mathematical equations. The results one can obtain from simulations may vary, depending upon how the simulation is handled. The computer treats the analytical formulae like a theoretical physicist fond of manipulating. Instead, many bits of numbers are crunched by the computer. Consequently, one can get only a single event instead of a physical law out of the computer. To learn the general behavior and laws of nature, we have to interpret and analyze the computer results. Numerical work is rarely used to uncover new fundamental laws of nature, and in this respect computational science is fundamentally different from theoretical science. However, computer simulations can be used to discover previously unknown phenomena. In this respect, computations are like physical experiments whose results depend on initial and boundary conditions. Moreover, like the laboratory experimenter, the computational researcher has to perform a large number of numerical experiments. Luckily, the simulation is fully repeatable so one can get a feel for the general behavior of a natural system and learn something new while changing the conditions of the experiment. As numerical methods improve and computing power in both speed (more than $9 \cdot 10^9$ floating point operations per a second in a single unit) and storage (more than 70 GB on a single disk) is increasing rapidly, simulations become more accurate conferring computational physics its significance. The variety of complex flows that computational fluid dynamics can analyze continues to increase. Nevertheless, the solutions to much more complex flows are desired.

However, numerical modelling has its limitations. The conditions investigated numerically are usually much simpler than those encountered in nature. Even the most powerful present supercomputers can handle a finite number of degrees of freedom. Both the finiteness of the capacity of computer memory and the finiteness of operation speed, force the physical systems that are described by computational physics to be represented by a discrete finite mathematics. On the other hand, as the power of computers has been increasing at an exponential rate we expect a computer will become a more and more powerful tool in the future.

In the present paper we describe various numerical methods which can be used to solve a variety of fluid equations. Section 2 presents the advection equation which can be numerically solved by the use of modern shock-capturing schemes. Sections 3 and 4

provide a short review of old and modern shock-capturing schemes. Moreover, in Section 4 wave propagation method is briefly described. Section 5 discusses multi-dimensional schemes. In the forthcoming Section we present a model which can precisely represent the real phenomena by a numerical scheme. As an approach to the problem we adapt a modern numerical code that solves the Euler equations which describe the dynamics of pollutants and ambient air. Such model is expected to give more adequate results than a model based on a single advection equation. We describe this model in Section 6. In Section 7 an example of the performance of a modern hydrodynamic code in the case of simulations of air-pollutants which are emitted continuously from a linear emitter into the ambient air is provided. The paper is concluded with a short summary of the main results.

2. Advection equation and air-pollutants

Dynamics of air-pollutants with the mass density $q(x,t)$ and the constant wind speed v can be described by the advection equation (*e.g.* [2]):

$$\frac{\partial q}{\partial t} + v\frac{\partial q}{\partial x} = 0, \quad -\infty < x < \infty, \quad t \geq 0, \quad v = const., \tag{1}$$

with the initial ($t = 0$) condition

$$q(x,0) = q_0(x). \tag{2}$$

Here, x is the spatial variable and t is the time. The solution of the above initial-value problem is:

$$q(x,t) = q(x - vt, 0). \tag{3}$$

That is, the initial profile of air-pollutants is simply translated with a vector vt without any change in shape.

2.1. Old shock capturing schemes for the advection equation

The history of the development of numerical schemes for Equation (1) is long and rich. The idea that shock-capturing can be accomplished through an appropriate dissipation term was used in early shock-capturing schemes. We explain it in some details below.

We discretize the $x - t$ plane by choosing a mesh width Δx and a time step Δt, and define discrete mesh points (x_i, t_n) by:

$$x_i = i\Delta x, \quad i = \dots, -2, -1, 0, 1, 2, \dots, \quad t_n = n\Delta t, \quad n = 0, 1, 2, \dots. \tag{4}$$

A forward Euler scheme leads to the discretization of the temporal derivative, *viz.*

$$\left.\frac{\partial q}{\partial t}\right|_{i,n} = \frac{q_i^{n+1} - q_i^n}{\Delta t} + 0(\Delta t). \tag{5}$$

Here, $0(\Delta t)$ denotes all terms which are proportional to Δt. As a consequence of that scheme (5) is first-order accurate in time.

A centered Euler scheme, which is second-order accurate in space, can be used for a discretization of the spatial derivative:

$$\left.\frac{\partial q}{\partial x}\right|_{i,n} = \frac{q_{i+1}^n - q_{i-1}^n}{2\Delta x} + 0\left((\Delta x)^2\right). \tag{6}$$

Then, the resulting scheme to Equation (1) is:

$$\frac{q_i^{n+1} - q_i^n}{\Delta t} = -v\frac{q_{i+1}^n - q_{i-1}^n}{2\Delta x}. \tag{7}$$

This equation can be rewritten as:

$$q_i^{n+1} = q_i^n - \frac{1}{\Delta x}(F_{i+1/2}^n - F_{i-1/2}^n), \tag{8}$$

where the numerical flux F is an approximation to the integral that is evaluated at the cell interface $x_{i+1/2}$, *i.e.*:

$$F_{i+1/2}^n = \int_{t_n}^{t_{n+1}} vq(x_{i+1/2},t)dt = 1/2\int_{t_n}^{t_{n+1}} v(q_{i+1}^n + q_i^n)dt. \tag{9}$$

The above scheme is called *explicit* as the fluxes on the right-hand side of Equation (8) are expressed by known quantities which were already computed at old time $t_n = n\Delta t$. Unfortunately, this scheme is unconditionally unstable and therefore it is useless in practice. See Section 2.3 for the stability analysis of Equation (8).

A stable scheme can be obtained if q^n in the flux F in (8) is replaced by new, and therefore unknown, density q^{n+1} that is evaluated at $t_{n+1} = (n+1)\Delta t$. Then, we get an *implicit* scheme, *viz.*

$$q_i^{n+1} = q_i^n - \frac{1}{\Delta x}(F_{i+1/2}^{n+1} - F_{i-1/2}^{n+1}). \tag{10}$$

Another way of getting a numerically stable scheme is to replace q_i^n in Equation (8) by its average:

$$q_i^n \rightarrow \frac{q_{i-1}^n + q_{i+1}^n}{2}. \tag{11}$$

This turns into the *Lax-Fredrichs* scheme:

$$q_i^{n+1} = \frac{q_{i-1}^n + q_{i+1}^n}{2} - \frac{1}{\Delta x}(F_{i+1/2}^n - F_{i-1/2}^n), \tag{12}$$

which in the form of discretization (7) is exactly the representation of the following equation:

$$\frac{\partial q}{\partial t} + v\frac{\partial q}{\partial x} = \frac{(\Delta x)^2}{2\Delta t}\frac{\partial^2 q}{\partial x^2}. \tag{13}$$

We have, in effect, added a diffusion term to the advection equation. The Lax-Fredrichs scheme is thus said to introduce a numerical dissipation. This scheme belongs to a family of old shock-capturing schemes.

From Equation (13), we see that the essence of old shock-capturing schemes is to smear large-gradient profiles, such as occur at shocks, over a small number of grid points. The smearing is done by introducing into the system a sufficient amount of a linear dissipation which is implemented globally, both in high-gradient regions and low-gradient regions.

Our purpose now is to develop a modern scheme which will resolve a shock over few grid points. However, before doing that, we will introduce some basic information about numerical errors, stability analysis and monotonicity.

2.2. Numerical errors

We will introduce the following definitions:

Discretization error is the difference between the exact analytical solution of the partial differential equation (such as Equation (1)) and the exact (round-off free) solution of the corresponding difference equation (*e.g.* Equation (7));

Round-off error is the numerical error that is introduced after a repetitive number of calculations.

We define: $A \equiv$ analytical solution of the partial differential equation, $D \equiv$ exact solution of the difference equation, $N \equiv$ numerical solution from a computer. Then:

$$\text{Discretization error} = A - D,$$
$$\text{Round-off error} = N - D.$$

Round-off errors occur as a result of:

Numerical diffusion that is associated with a finite length of a numerical cell. The numerical diffusion is large for short waves ($k_x \Delta x \gg 1$), which are removed from the system. Here, k_x is the wavevector. The diffusion controls all the errors mentioned below;

Numerical dispersion that is revealed by the fact that waves of different wavelengths propagate with different speeds. The dispersion is usually larger for shorter waves ($k_x \Delta x \gg 1$);

Nonlinear instabilities which are generated by a nonlinear term such as $V \frac{\partial V}{\partial x}$. This term transforms energy from long wavelengths to short wavelengths for which dispersive errors are higher;

Gibbs error which is revealed by short oscillations. The Gibbs error is a consequence of finite Fourier spectrum which is a result of discretization of a continuous medium;

Spurious modes: Equation (7) admits at steady state ($\frac{\partial q}{\partial t} = 0$) apart from the physical mode $q_i^n = q_0 = const.$ the spurious mode $q_i^n = q_0(-1)^i$. This mode decouples the odd and even mesh points. It can be eliminated from the system by coupling the odd and even nodes or by introducing a numerical diffusion. Occurrence of spurious modes is a consequence of dispersive errors;

Overshoots and undershoots: Consider the Cauchy problem for Equation (7) with $v > 0$, *viz.*

$$q_i^0 = \begin{cases} 0, & i \le I, \\ 1, & i > I. \end{cases} \tag{14}$$

The spatial derivative $\frac{\partial q_I}{\partial x} > 0$ at $x = I \Delta x$. Then, according to Equation (7) $\frac{\partial q_I}{\partial t} < 0$ and therefore q_I will decrease in time, producing an unphysical undershoot at $x = I \Delta x$. This undershoot is usually accompanied by an overshoot which occurs at $x = (I+1)\Delta x$.

2.3. Von Neumann stability analysis

Numerical errors lead to perturbations of a true solution. If this solution is unstable with respect to perturbations, there is an energy transfer to them and they grow quickly in time, deteriorating the solution.

To check whether a numerical scheme is stable in the *von Neumann* sense we introduce a Fourier mode

$$q_j^n = \xi^n e^{ikj\Delta x}, \tag{15}$$

where k is a wave-vector and $\xi = \xi(k)$ is a complex function of k, called the *amplification factor*.

A numerical scheme is *unstable* if $|\xi(k)| > 1$ for some k. To find $\xi(k)$ for Equation (7), we substitute (15) back into (7). Dividing by ξ^n, we get:

$$\xi(k) = 1 - i \frac{v\Delta t}{\Delta x} \sin(k\Delta x).$$

Hence, $|\xi(k)| > 1$ for all k. So, discretization (7) is unconditionally unstable.

2.4. Monotonicity

As a consequence of numerically induced oscillations, an important problem is to develop a scheme which leads to monotonic solutions.

A grid function is called monotonic if the following condition is satisfied:

$$\min(q_{i-1}, q_{i+1}) \leq q_i \leq \max(q_{i-1}, q_{i+1}).$$

This condition prevents an occurrence of local maxima or minima at q_i. A numerical scheme is monotonicity preserving if a monotonic function at $t = n\Delta t$ will be kept monotonic at $t = (n+1)\Delta t$. Monotonic schemes do not accentuate local maxima and local minima are non-decreasing.

To measure the monotonicity, Total Variation is defined as follows:

$$TV(q) = \int_{-\infty}^{\infty} \left| \frac{\partial q}{\partial x} \right| dx \simeq \sum_{i=-\infty}^{\infty} |q_i^n - q_{i-1}^n|.$$

The monotonicity condition is:

$$TV(q^{n+1}) \leq TV(q^n).$$

A numerical scheme satisfying this condition is called a Total Variation Diminishing scheme. Such scheme is monotonicity preserving as it eliminates oscillations which occur near steep profiles [3, 4]. That means that if the initial data are free of oscillations, then the solution should be monotonous for later times.

3. Modern shock-capturing schemes for the advection equation

Modern shock-capturing schemes are intelligent as they add only enough dissipation in small localized regions to eliminate numerical oscillations. To achieve this the dissipation has to be nonlinear and implemented locally, at regions of high-gradients. Consequently, the schemes reduce to some highly dissipative, first-order schemes when the solutions are discontinuous and to some minimally dissipative, higher-order scheme when the solution is smooth. The dissipation is added only for those wavelengths that the high-order scheme cannot resolve. As a consequence of that, the shock is captured over a small number of points and without any oscillations.

3.1. Upwind schemes

A key point of modern shock-capturing schemes is upwind differencing which stabilizes shocks and other large gradient profiles. An upwind scheme for advection Equation (1) can be written as:

$$q_i^{n+1} = q_i^n - \frac{\Delta t}{\Delta x} v \Delta q^n, \tag{16}$$

where:

$$\Delta q^n = \begin{cases} q_{i+1}^n - q_i^n, & \text{if } v < 0, \\ q_i^n - q_{i+1}^n, & \text{if } v > 0. \end{cases}$$

Modern shock-capturing schemes can be divided into geometric approaches and algebraic approaches. While all of the members of the geometric approaches attempt to assign a value to the generalized density, q, in a global manner the algebraic approaches use flux limiters. Some common limiters are: minmod, superbee, van Leer, and monotonized centered [5].

The algebraic schemes enforce some constraint on the problem, usually that some component of the solution be total variation diminishing (*e.g.* [4]). The geometric approaches are: the Godunov scheme [6], MUSCL scheme [7], piecewise parabolic method (PPM) scheme (*e.g.* [8]), and essentially non-oscillatory (ENO) scheme [9–11]. In the geometric approaches the defining functions can be continuous within a cell, but may be discontinuous at cell edges. For example, in the original Godunov approach [6], the solution was considered to be piecewise constant over each grid cell at a fixed time. The evolution of the flow to the next time step results from the waves interactions originating at adjacent cell boundaries, specifically a Riemann initial-value problem (*e.g.* [12]).

3.2. Riemann problem

In the Riemann problem, an imaginary membrane, which separates two cells at different states is ruptured, and shock, contact, and expansion waves are emitted when these two states interact. In other words the Riemann solver is based on the idea that two adjacent arbitrary states will evolve into a set of left- and right-going shocks and rarefactions. We can explain this more precisely by considering the initial condition:

$$q(x,0) = \begin{cases} q_l, & x < 0, \\ q_r, & x \geq 0, \end{cases} \tag{17}$$

for the equation:

$$\frac{\partial q}{\partial t} + \frac{\partial f(q)}{\partial x} = 0. \tag{18}$$

Here, q_l and q_r are constants corresponding to the left and right states, respectively. With certain assumptions on the flux function $f(q)$, it is always possible, in principle, to solve the Riemann problem if the states q_l and q_r are sufficiently close to each other. The solution consists of waves traveling with finite velocities. These waves may either be discontinuous shock waves or smooth rarefactions. The procedure for constructing the solution of a Riemann problem is called a Riemann solver. The most popular Riemann solver is due to Roe [13].

3.3. Roe solver

The keystone of the Roe scheme [13] is the introduction of an average Jacobian A_v, which approximates the Jacobian $A = \frac{\partial f}{\partial q}$, associated with Equation (18).

The average Jacobian (called also the Roe matrix) is such that for any given left and right pair of states (q_l, q_r) the so-called Property U is satisfied:

  (i) A_v is a linear mapping from the vector space q to the vector space f;

 (ii) $A_v(q_l, q_r) \rightarrow \dfrac{\partial f}{\partial q}$ as q_l and $q_r \rightarrow q$;

(iii) $A_v(q_l, q_r)$ has real eigenvalues and a complete set of linearly independent eigenvectors;

 (iv) $A_v(q_r - q_l) = f_r - f_l$ for any q_l and q_r.

In the case of Euler or magnetohydrodynamic equations, average mass density is given by [12]:

$$\rho_v = \sqrt{\rho_l \rho_r} \tag{19}$$

and the rest of flow variables are averaged as follows:

$$\phi_v = \frac{\phi_l \sqrt{\rho_l} + \phi_r \sqrt{\rho_r}}{\sqrt{\rho_l} + \sqrt{\rho_r}}. \tag{20}$$

Once all the averaged variables are obtained, the linearized Riemann problem, expressed as:

$$\frac{\partial q}{\partial t} + A_v \frac{\partial q}{\partial x} = 0, \tag{21}$$

is considered at each interface. The exact solution of this approximate problem can be expressed in terms of right eigenvector r_i of A_v as:

$$\Delta q \equiv q_r - q_l = \sum_{i=1}^{m} \alpha_i r_i, \qquad \alpha_i = r_i^{-1} \Delta q. \tag{22}$$

From property (iv) it follows that the flux difference is given as:

$$\Delta f = \sum_{i=1}^{m} \alpha_i \lambda_i r_i. \tag{23}$$

3.4. The Godunov method and its generalizations

3.4.1. The Godunov scheme

In the original Godunov [6] approach upwind finite-volume flow solver was used. The solution was considered to be piecewise constant over each grid cell at a fixed time:

$$q(x) = q_i, \quad x_{i-1/2} < x < x_{i+1/2}. \tag{24}$$

So, discontinuities are placed at the cell interfaces $x_{i+1/2}$. Moreover, the Riemann problem at adjacent cell boundaries is solved. The Godunov method is first-order accurate in space.

3.4.2. MUSCL scheme

The low accuracy and the complexity of the Godunov method meant that other methods have mostly been used for a long time. Two decades passed until the Godunov approach was first extended to second-order spatial accuracy by the MUSCL approach

developed by van Leer [7]. In this scheme the accuracy was increased by constructing a piecewise linear approximation of $q(x)$ at the beginning of each time step, *viz.*

$$q(x) = q_i + s_i(x - \bar{x}_i), \quad x_{x-1/2} < x < x_{x+1/2}, \tag{25}$$

where $\bar{x}_i = (x_i + x_{i+1})/2$ and s_i is a slope. As an upwind (Beam-Warming) slope we can choose:

$$s_i = \frac{q_i - q_{i-1}}{\Delta x}.$$

In regions where $s_i = 0(1)$, the reconstruction used is linear, and the truncation error is $0\big((\Delta x)^2\big)$. In regions where $s_i = 0$, the reconstruction used is piecewise constant, and the truncation error is $0(\Delta x)$.

As the above slope can lead to oscillatory approximations to discontinuous solutions, slope-limiter methods may be introduced to reduce these oscillations and to enforce the monotonicity of the reconstruction.

3.4.3. Piecewise parabolic scheme

A piecewise parabolic method (PPM) scheme is an extension of the MUSCL scheme. The key difference from MUSCL is that $q(x,t)$ is allowed to be piecewise parabolic within a cell, rather than piecewise linear. Second-order accuracy in time is again achieved in the same way as in the MUSCL scheme, via characteristic tracing and solving Riemann problems. Dai and Woodward [12, 8] applied the PPM scheme to ideal magnetohydrodynamic equations.

3.4.4. Essentially non-oscillatory scheme

Essentially non-oscillatory (ENO) schemes are again extensions of the PPM approach. Arbitrarily high-order polynomials are allowed to define $q(x,t)$ within a cell, yielding arbitrarily high-order spatial accuracy [9–11].

It is noteworthy that various modern shock-capturing schemes were compared by Woodward and Colella [14] by computing a blast wave interaction problem in one dimension. The result of that test was an ordering of the schemes in terms of the accuracy. With the most accurate schemes listed first, that ordering was obviously as follows: PPM, MUSCL, and the Godunov scheme.

4. Wave propagation method as a modern shock-capturing scheme

In this part of the paper we consider the wave propagation method that was developed by [15] for a linear hyperbolic system of equations:

$$q_t + Aq_x = 0, \tag{26}$$

where the $m \times m$ matrix A has m right-eigenvectors r^p and real eigenvalues λ^p for $p = 1, 2, \ldots, m$, *viz.*

$$Ar^p = \lambda^p r^p, \quad p = 1, 2, \ldots, m.$$

Then, the difference of the generalized density vector Δq_i can be written as:

$$\Delta q_i \equiv q_i - q_{i-1} = \sum_{i=1}^{m} \alpha_i^p r^p \equiv \sum_{i=1}^{m} W_i^p, \tag{27}$$
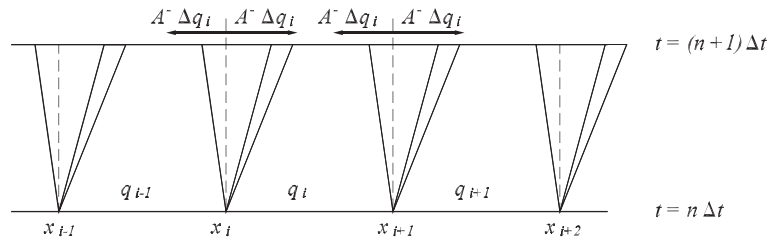
where W_i^p is the wave and λ^p is its speed.

The matrix A can be decomposed as:

$$A = R \Lambda R^{-1}, \tag{28}$$

where the matrices R and Λ are constructed by the right-eigenvectors r^p and eigenvalues λ^p, respectively, *viz.*

$$R = [r^1 | r^2 | \ldots | r^m], \qquad \Lambda = diag(\lambda^1, \ldots, \lambda^m). \tag{29}$$

Let q_i^0 denote the value at the interface between q_{i-1} and q_i. The case of $q_i > q_{i-1}$ is shown in Figure 1.

Figure 1. Waves, interface values and flux differences

Then, with the use of Equation (27) we can write:

$$q_i^0 - q_{i-1} = \sum_{\lambda_i^p < 0} W_i^p, \qquad q_i - q_i^0 = \sum_{\lambda_i^p > 0} W_i^p. \tag{30}$$

According to property (iv) of the Roe solver, the flux at the interface can be expressed twofold:

$$f(q_i^0) = A q_i^0 = A q_{i-1} + \sum_{\lambda_i^p < 0} \lambda_i^p W_i^p = A q_{i-1} + A^- \Delta q_i, \tag{31}$$

$$f(q_i^0) = A q_i^0 = A q_i - \sum_{\lambda_i^p > 0} \lambda_i^p W_i^p = A q_i - A^+ \Delta q_i, \tag{32}$$

where:

$$\Lambda^{\pm} = diag(\lambda^{p\pm}), \qquad A^{\pm} = R \Lambda^{\pm} R^{-1}, \tag{33}$$

$$\lambda^{p+} = \max(\lambda^p, 0), \qquad \lambda^{p-} = \min(\lambda^p, 0). \tag{34}$$

4.1. First-order scheme

Equation (26) can be discretized as:

$$q_i^{n+1} = q_i - \frac{\Delta t}{\Delta x}(F_{i+1} - F_i), \tag{35}$$

where the flux:

$$F_i = f(q_i^0) = A q_i^0. \tag{36}$$

Using (31) and (32), we obtain:

$$F_i = f(q_i) - A^+ \Delta q_i, \qquad F_{i+1} = f(q_i) + A^- \Delta q_{i+1}. \tag{37}$$

Equation (35) can now be rewritten as:

$$q_i^{n+1} = q_i - \frac{\Delta t}{\Delta x}(A^- \Delta q_{i+1} + A^+ \Delta q_i) \equiv q_i + \Delta_i^{upwind}. \tag{38}$$

This scheme is first-order accurate in space and is called the Godunov scheme.

4.2. Second-order correction

A second-order correction to Equation (38) is obtained by altering its right-hand side as:

$$q_i^{n+1} = q_i + \Delta_i^{upwind} - \frac{\Delta t}{\Delta x}(\bar{F}_{i+1} - \bar{F}_i), \tag{39}$$

where the flux:

$$\bar{F}_i = \frac{1}{2}\sum_{p=1}^{m}|\lambda_i^p|\left(1 - \frac{\Delta t}{\Delta x}|\lambda_i^p|\right)\bar{W}_i^p. \tag{40}$$

Here, $\bar{W}_i^p$ is a limited version of the wave W_i^p, obtained by comparing W_i^p to W_{i-1}^p if $\lambda_i^p > 0$ or to W_{i+1}^p if $\lambda_i^p < 0$.

4.3. Entropy fix

Godunov schemes are very robust in most situations. However, there are few instances in which a particular scheme produces inappropriate results [16, 17]. For example, when computing rarefaction waves, the scheme can produce nonphysical expansion shocks in the computed flow. This can lead to numerical approximations with entropy violating discontinuities. To prevent these expansion shocks, an intermediate state (that simulates the diffusion) between the left and right states is introduced [18]. This procedure is called an entropy fix and it is necessary to obtain physically relevant numerical approximations of the exact solution. In Roe method [13] the entropy fix is only required for the case of sonic rarefactions for which $\lambda_{il} < 0$ to the left of the wave while $\lambda_{ir} > 0$ to the right of the wave.

The idea used in the entropy fix is to replace the single jump $q_{jr} - q_{jl}$ propagating at speed λ_j by two jumps propagating at speeds λ_{jl} and λ_{jr}, with a new state q_{jn} in between.

The flux difference can be expressed as follows:

$$f(q_{jl}) - f(q_{jr}) = f(q_{jl}) - f(q_{jn}) + f(q_{jn}) - f(q_{jr}). \tag{41}$$

Using the property (iv) of the Roe solver this formula can be rewritten as:

$$\lambda_j(q_{jl} - q_{jr}) = \lambda_{jl}(q_{jl} - q_{jn}) + \lambda_{jr}(q_{jn} - q_{jr}). \tag{42}$$

Hence,

$$q_{jn} = \frac{(\lambda_j - \lambda_{jl})q_{jl} + (\lambda_{jr} - \lambda_j)q_{jr}}{\lambda_{jr} - \lambda_{jl}} \tag{43}$$

and consequently

$$q_{jn} - q_{jl} = \frac{\lambda_{jr} - \lambda_j}{\lambda_{jr} - \lambda_{jl}}(q_{jr} - q_{jl}) \equiv \frac{\lambda_{jr} - \lambda_j}{\lambda_{jr} - \lambda_{jl}}\alpha_j r_j, \tag{44}$$

$$q_{jr} - q_{jn} = \frac{\lambda_j - \lambda_{jl}}{\lambda_{jr} - \lambda_{jl}}(q_{jr} - q_{jl}) \equiv \frac{\lambda_j - \lambda_{jl}}{\lambda_{jr} - \lambda_{jl}}\alpha_j r_j. \tag{45}$$

The flux can now be written twofold:

$$F(q_l, q_r) = f(q_l) + \sum_{i \neq j}\lambda_i^- \alpha_i r_i + \hat{\lambda}_{jl}\alpha_j r_j \tag{46}$$

or

$$F(q_l, q_r) = f(q_r) - \sum_{i \neq j}\lambda_i^+ \alpha_i r_i - \hat{\lambda}_{jr}\alpha_j r_j, \tag{47}$$

where we introduced the following notation:

$$\hat{\lambda}_{jl} = \lambda_{jl}\frac{\lambda_{jl} - \lambda_j}{\lambda_{jr} - \lambda_{jl}}, \qquad \hat{\lambda}_{jr} = \lambda_{jr}\frac{\lambda_j - \lambda_{jl}}{\lambda_{jr} - \lambda_{jl}}. \tag{48}$$

Another deficiency of most Godunov-type schemes is the generation of a long wavelength noise, downstream nearly stationary shock. This noise is not effectively damped by the dissipation of the scheme [16].

4.4. An example – the isothermal hydrodynamic equations

The isothermal equations can be written as follows:

$$\frac{\partial \rho}{\partial t} + \frac{\partial (\rho u)}{\partial x} = 0, \tag{49}$$

$$\frac{\partial (\rho u)}{\partial t} + \frac{\partial (\rho u^2 + c^2 \rho)}{\partial x} = 0, \tag{50}$$

$$c = const., \qquad p = c^2 \rho. \tag{51}$$

For the Roe solver we define an average velocity [15]:

$$\bar{u}_i = \frac{\sqrt{\rho_{i-1}} u_{i-1} + \sqrt{\rho_i} u_i}{\sqrt{\rho_{i-1}} + \sqrt{\rho_i}}. \tag{52}$$

Then, from Equations (49) – (51) it follows that an average Jacobian (the Jacobian matrix $f'(q)$ evaluated at the averaged state) is:

$$A_i = \begin{pmatrix} 0 & 1 \\ c^2 - \bar{u}_i^2 & 2\bar{u}_i \end{pmatrix}. \tag{53}$$

The matrix A_i can be decomposed as:

$$A_i = R_i \Lambda_i R_i^{-1},$$

where:

$$R_i = \begin{pmatrix} 1 & 1 \\ \bar{u}_i - c & \bar{u}_i + c \end{pmatrix}, \quad \Lambda_i = \begin{pmatrix} \bar{u}_i - c & 1 \\ 0 & \bar{u}_i + c \end{pmatrix}, \quad R_i^{-1} = \frac{1}{2c} \begin{pmatrix} \bar{u}_i + c & -1 \\ -\bar{u}_i + c & 1 \end{pmatrix}. \tag{54}$$

The wave strengths are given by the following formulae:

$$\alpha_i = R_i^{-1} \Delta q_i, \tag{55}$$

$$\alpha_i^1 = \frac{1}{2c} [(\bar{u}_i + c) \Delta q_i^1 - \Delta q_i^2], \tag{56}$$

$$\alpha_i^2 = \frac{1}{2c} [(-\bar{u}_i + c) \Delta q_i^1 + \Delta q_i^2]. \tag{57}$$

The Riemann solver is determined by:

$$W_i^p = \alpha_i^p r_i^p, \quad p = 1, 2, \tag{58}$$

$$\lambda_i^1 = \bar{u}_i - c, \quad \lambda_i^2 = \bar{u}_i + c, \tag{59}$$

$$A_i^- \Delta q_i = \lambda_i^{1-} \alpha_i^1 r_i^1 + \lambda_i^{2-} \alpha_i^2 r_i^2, \tag{60}$$

$$A_i^+ \Delta q_i = \lambda_i^{1+} \alpha_i^1 r_i^1 + \lambda_i^{2+} \alpha_i^2 r_i^2. \tag{61}$$

To check for a transonic rarefaction, we compute:

$$\hat{q}_i = q_{i-1} + \alpha_i^1 r_i^1 = q_i - \alpha_i^2 r_i^2. \tag{62}$$

Suppose that:

$$u_{i-1} - c < 0 < \hat{u}_i - c. \tag{63}$$

Then, there may be a transonic rarefaction in the first wave and the flux differences are modified according to formulae (46) and (47) as follows:

$$A^- \Delta q_i = \frac{(\hat{u}_i - c) - (\bar{u}_i - c)}{(\hat{u}_i - c) - (\bar{u}_{i-1} - c)} (u_{i-1} - c) W_i^1, \tag{64}$$

$$A^+ \Delta q_i = [f(q_i) - f(q_{i-1})] - A^- \Delta q_i. \tag{65}$$

5. **Multi-dimensional schemes**

A common approach when solving multi-dimensional hyperbolic equations is to apply operator splitting method (*e.g.* [19]). The idea of this method is to iterate sequentially one-dimensional equations. The popularity of this method is a consequence of the fact that the numerical schemes lead to surprisingly good results (*e.g.* [20]) and that the strategy is very simple as any multi-dimensional scheme consists of a system of the one-dimensional problems. However, the operator splitting methods have several disadvantages. For example, discontinuities traveling obliquelly to the grid are smeared more than those traveling in the coordinate directions. The implementation of boundary conditions may also be complicated using this method.

In unsplit methods, information is propagated in a genuinely multi-dimensional way. One-dimensional Riemann problems are solved at the interfaces and limiter functions are applied to suppress numerically induced oscillations which are usually generated by higher-order derivative terms. The left-going and right-going waves are split into parts propagating in the transverse direction by solving Riemann problems in coordinate directions tangential to the interfaces. These cross-derivative terms are necessary for obtaining both a stable and second-order schemes [21].

A class of conservative finite difference schemes for hyperbolic conservation laws in multi-dimensional spaces has been developed by [22]. These schemes do not make use of operator splitting and instead the multidimensional wave properties of the solution are used to calculate fluxes. In these schemes some of the second-order terms are limited to suppress oscillations. Although the same Riemann problems appear in these schemes as in the operator split methods, these schemes are somewhat more expensive, requiring twice as many solutions to the Riemann problems as the corresponding operator split algorithm.

6. **Model of air-pollutants**

Dynamics of air-pollutants can be described by the hydrodynamic equations:

$$\frac{\partial \rho}{\partial t} + \nabla \cdot (\rho \mathbf{V}) = S_\rho + S_D, \tag{66}$$

$$\frac{\partial (\rho \mathbf{V})}{\partial t} + \nabla \cdot [(\rho \mathbf{V}) \mathbf{V}] = -\nabla p + \rho g \hat{y} + \mathbf{S_V}, \tag{67}$$

$$\frac{\partial p}{\partial t} + \nabla \cdot (p \mathbf{V}) = -(\gamma - 1) p \nabla \cdot \mathbf{V} + S_p, \tag{68}$$

where ρ is the mass density, $\mathbf{V}$ is the velocity, p is the gas pressure, g is the gravity, $\hat{y}$ is a unit vector in the vertical direction y, and t denotes the time. The adiabatic constant that is

expressed by the ratio of specific heats $\frac{c_p}{c_V}$ is γ. The x-axis lies in the horizontal direction. Henceforth, we consider the two-dimensional case with $\frac{\partial}{\partial z} = 0$. S_D is a diffusive term:

$$S_D = -\nabla \cdot D(x, y, t, \rho) \nabla \rho(x, y, t). \tag{69}$$

Assuming the diffusive coefficient D to be a constant, the latter equation can be rewritten as follows:

$$S_D = -D\nabla^2 \rho. \tag{70}$$

The source terms S_ρ, $\mathbf{S_V}$ and S_p are associated with the emission of the pollutants. These terms are derived in the following way. In the diffusion-free case ($D = 0$) the mass continuity equation can be written as:

$$\frac{\partial \rho}{\partial t} + \nabla \cdot (\rho \mathbf{V}) = -\nabla(\rho_e \mathbf{V_e}) \equiv S_\rho, \tag{71}$$

where ρ_e and $\mathbf{V_e}$ denote the mass density and velocity of the emitted pollutants, respectively. In the case of a vertical emission with the speed $\mathbf{V_e} = [0, \tilde{V}_{ey}]$, the mass source term is given by:

$$S_\rho = -\frac{\partial}{\partial y}(\rho_e \tilde{V}_{ey}). \tag{72}$$

If the emittor of its width x_0 is placed at $y = y_0$, the parameters of the emission that takes place for $y > y_0$ are described as follows:

$$\rho_e = \hat{\rho}_e e^{-\frac{y-y_0}{x_0}}, \quad \tilde{V}_{ey} = const. \tag{73}$$

As a consequence of that the source term S_ρ is described by the following expression:

$$S_\rho = \tilde{V}_{ey} \frac{\hat{\rho}_e}{x_0} e^{-\frac{y-y_0}{x_0}} = \frac{E}{A \cdot x_0} e^{-\frac{y-y_0}{x_0}}, \tag{74}$$

where $E = \hat{\rho}_e \tilde{V}_{ey} A$ is the flux of the pollutants which cross the area A of the emitter. Having defined the mass source term, the remaining source terms $\mathbf{S_V}$ and S_p are given as:

$$\mathbf{S_V} = S_\rho \tilde{V}_{ey} \hat{y}, \tag{75}$$

$$\mathbf{S_p} = \frac{p_e}{\gamma - 1} \tilde{V}_{ey}. \tag{76}$$

7. Numerical simulations of air-pollutants

This research is stimulated by an elementary disagreement between the results obtained with the use of the existent air-pollution models and the experimental data. Our approach is to adapt a modern numerical scheme that solves a set of the hydrodynamic equations which describe the dynamics of pollutants in the ambient air. Such a model is expected to represent more adequately physical phenomena which take place in the Earth's atmosphere than a model based on a single equation.

Numerical simulations which are presented in this paper treat pollutants which are emitted from a linear smokestack into the ambient air. At this stage, wind and topography of a terrain are neglected and the atmosphere is assumed to be isothermal. Such approximations allow to trace the distribution of pollutants in the neighbourhood of an emittor as well as observe a plume development. These simulations consist a continuation of the work led so far by the authors [23, 24].

7.1. The numerical scheme

In the present research we have applied the CLAWPACK (Conservation LAWs PACKage) code which is a collection of Fortran routines for solving a hyperbolic system of conservation laws. The general structure of the code is described in detail in the user notes report [1]. Here, we briefly describe the method applied in the code.

For the numerical purposes, the Euler equations can be written in the conservative form:

$$\frac{\partial}{\partial t} \begin{bmatrix} \rho \\ \rho V_x \\ \rho V_y \\ E \end{bmatrix} + \frac{\partial}{\partial x} \begin{bmatrix} \rho V_x \\ \rho V_x^2 + p \\ \rho V_x V_y \\ V_x(E+p) \end{bmatrix} + \frac{\partial}{\partial y} \begin{bmatrix} \rho V_y \\ \rho V_x V_y \\ \rho V_y^2 + p \\ V_y(E+p) \end{bmatrix} = \mathbf{S}, \tag{77}$$

where $\mathbf{S}$ denotes the source vector, and the total energy density is $E = \frac{1}{2}\rho(V_x^2 + V_y^2) + p/(\gamma - 1)$. The method used here, is a finite-volume method on a uniform rectangular grid Δx, Δy. In two dimensions Equation (77) can be discretized as follows:

$$U_{i,j}^{n+1} = U_{i,j}^n - \Delta t \left[\frac{1}{\Delta x} \left(F_{i+1/2,j} - F_{i-1/2,j} \right) + \frac{1}{\Delta y} \left(G_{i,j+1/2} - G_{i,j-1/2} \right) \right], \tag{78}$$

where $U_{i,j}^n$ is an average of $q(x = i\Delta x,\ y = j\Delta y,\ t = n\Delta t)$ over the cell (i, j), F and G are numerical fluxes that are evaluated at cell interfaces to properly resolve the wave structure. The waves arising from a solution of Equation (78) are then used to define second-order correction terms, typically with the application of limiters to suppress numerically induced oscillations. In this two-dimensional scheme a transverse splitting of the waves is also used to improve stability and resolution.

The CLAWPACK code uses a modern shock wave propagation method [15]. These waves are the solution of hyperbolic differential Equations (77). Additionally, a Riemann solver which decomposes data at cell edges into a set of waves and wave speeds, is adapted. To suppress numerically induced oscillations, flux limiters are used.

Problems with source terms $\mathbf{S}(u)$ are generally solved using the Godunov splitting in which the solution of the homogeneous equation, $\frac{\partial u}{\partial t} + \frac{\partial (f(u))}{\partial x} + \frac{\partial (g(u))}{\partial y} = 0$, is alternated with solutions of the equation $\frac{\partial u}{\partial t} = \mathbf{S}(u)$. An exception is the gravity source term that is treated by the method which was developed by LeVeque [25]. This method is essentially based on an implementation of a Riemann problem at the center of each grid cell whose flux difference exactly cancels the source term. Such approach has no problem with preserving steady states and it accurately calculates small perturbations of such states.

7.2. Boundary conditions

The proper treatment of the boundary conditions at the edges of the simulation domain is not a trivial aspect of time-dependent numerical simulations. The boundary conditions must represent the rest of the physical system and do not reflect any disturbances going out of the numerical domain and must pass information about the physical system. An important problem is associated with open boundary conditions. Incorrectly treated open boundary conditions lead to artificial reflection of the wave at the boundaries. A commonly applied method is known as the Sommerfeld radiation condition [26].

A simple method for imposing boundary conditions is to generate image cells at the boundaries of the simulation region and then, to apply the Riemann solver to compute the flux across these boundaries. This treatment is very easily implemented in an explicit

scheme in which the fluid variables in the image cells are set at the beginning of each time step. For implicit schemes, this approach can also be used although for large time step a considerable time lag between the solutions and the boundary conditions can lead to numerical instabilities.

In the CLAWPACK code two ghost cells are generated at each side of the computational domain, which in the case of the present approach is divided into uniform grid of 133 cells in the x-direction and 133 cells in the y-direction. The boundaries of the simulation box are placed at $x = \pm 10\, x_0$, $y = 0$, and $y = 20\, x_0$, where x_0 is the width of an emittor. The height of the emittor has been assumed to be $10\, x_0$. The top, left and right boundaries are in the present model entirely open. So, any signal can easily cross through them. The bottom boundary, however, corresponds to a rigid wall. Consequently, when a signal reaches the bottom boundary, it is reflected off and eventually spread near the surface of the Earth.

7.3. Initial conditions

Initially, at $t = 0$, density and pressure correspond to the isothermal atmosphere of its temperature $T_0 = 293$ K. The vertical profiles of the atmosphere are presented schematically in Figure 2. We assumed the ground pressure $p_0 = 101325$ Pa and the mass density $\rho_0 = 1.29\, \text{kg/m}^3$. These values provide the sound speed $c_s = 333$ m/s. The diffusion coefficient was assumed to be constant, $D = 0.333 \cdot 10^{-4}\, \text{m}^2/\text{s}$.
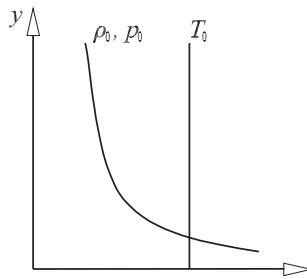
Figure 2. Equilibrium profiles of the mass density, pressure and temperature for the case of the isothermal atmosphere

The outlet from a smokestack is localized at the position $|x| < x_0 = 1$ m and the height $y_0 = 10\, x_0$ above the Earth's surface. The emission is specified by introducing the source components of the mass density, velocity and pressure in Equations (66) – (68). Six numerical sessions were performed for the mass density of the emitted pollutants: a) $\rho_e = 2.0\, \rho_0$, b) $\rho_e = 1.5\, \rho_0$, c) $\rho_e = 1.0\, \rho_0$, d) $\rho_e = 0.75\, \rho_0$, e) $\rho_e = 0.1\, \rho_0$, and f) $\rho_e = 0.002\, \rho_0$. The emitted pollutants are chosen five times hotter than the ambient air, and they possess the initial vertical velocity $\tilde{V}_{ey} = 15$ m/s.

7.4. Numerical results and discussion

We describe first the results of numerical simulations in the case of $\rho_e/\rho_0 = 2.0$ and $\rho_e/\rho_0 = 1.5$. Our purpose here is to examine the behaviour of dense pollutants in the gravitational field. Neglecting shapes and dimensions of gas particles, the emitted pollutants can be approximately treated as dust.

Figure 3a shows that the emitted dense gas spreads essentially in the horizontal direction. This spreading is also discernible in Figure 3b which shows the velocity vectors
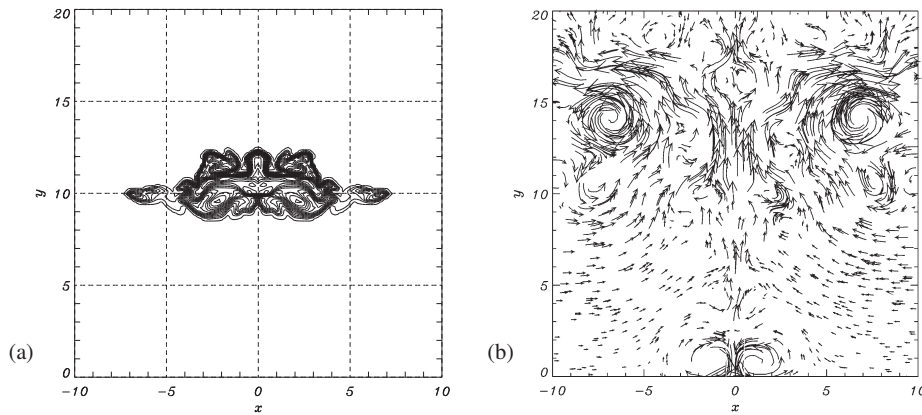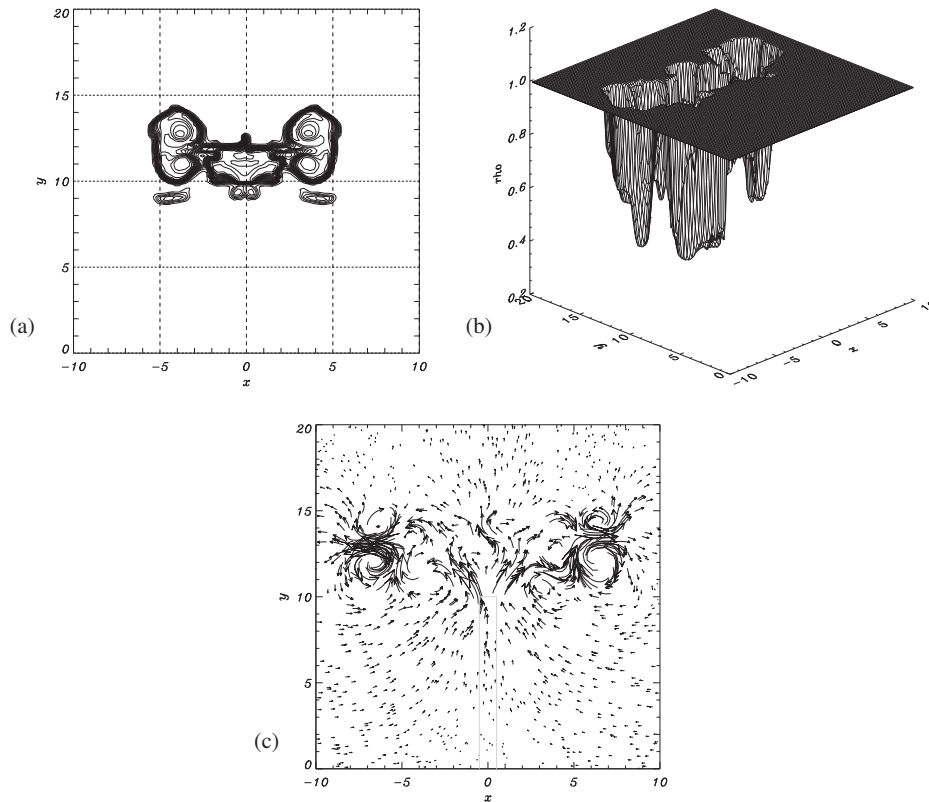
Figure 3. Spatial distribution of pollutants in the case of $\rho_e = 1.5\,\rho_0$: (a) the mass density at $t = 0.75\,\text{s}$; (b) the velocity vectors at $t = 3.75\,\text{s}$

at $t = 3.75\,\text{s}$. We observe here a generation of vortices which are convected upwards at a later time. As a result of a high emission momentum and a buoyancy force these vortices pass a long distance.

It is worth mentioning that the ambient air provides a resistance for an expansion of the emitted pollution. This effect can be well observed at the initial stage of the emission (Figure 3a), when the expansion in the horizontal direction dominates over the vertical expansion. Later on, however, the emitted flux of pollution overcomes the resistance of the ambient air. As long as this flux possesses sufficiently large kinetic energy, the cloud of the pollution moves easily upwards at the initial stage (Figure 3b). However, at a later time the gravitational field takes over the buoyancy force, resulting in a fact that a cloud of pollution does not move along a straight line but along a bow (Figure 3b) and finally falls down (not shown in the figure).

The obtained results indicate that the effect of gravitation (*i.e.* a gravitational fall down of the pollution) is best seen at the initial phase of the emission when the highest damping of the pollution occurs. In the already disturbed air, however, spreading of pollutants is much easier both in the horizontal and vertical directions. We can find a confirmation of that in Figure 3b in which at $x = 0$ and $y = 12\,x_0$ we see a stream of vertically propagating pollutants. It is only at a certain height that the direction of these vectors changes and they deflect from the main vertical direction. Furthermore, in Figure 3b the arrangement of these vectors in the neighbourhood of the largest vortices (*e.g.*, at $x = 7\,x_0$ and $y = 10\,x_0$) indicates that at a certain distance from a smokestack we expect to observe a gravitational fall down of these pollutants. Small vortices are also generated at the sides of the outlet of the chimney. These vortices are pulled down by the gravity at the initial stage of their evolution. In Figure 3b such vortices are located at $x = y = 0$. The other falling down vortices are seen at $x = 0$ and $y = 4\,x_0$.

The case of $\rho_e = \rho_0$ is presented in Figure 4. It is interesting that in this case we do not observe any formation of a cloud of pollutants above the outlet from the smokestack. Instead, the plume expands into the horizontal direction, symmetrically on both sides of the chimney (Figure 4a). This case results in a rapid decrease (with a height from the chimney) of the density of the pollutants.
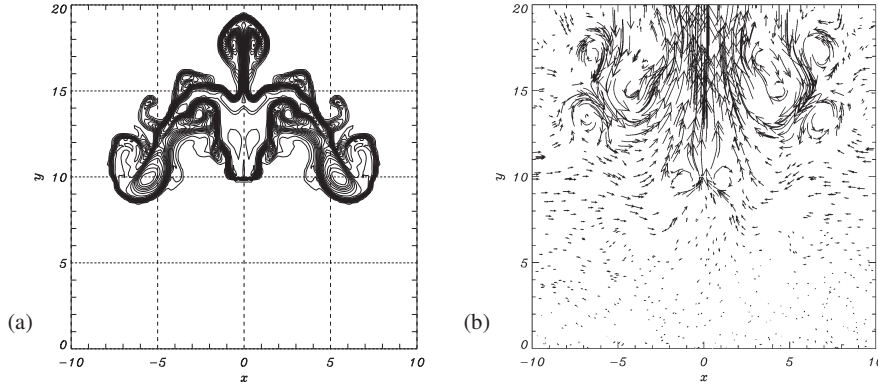
Figure 4. Spatial distribution of pollutants in the case of the emission density ρ_e equals to the ambient air density ρ_0, *i.e.* $\rho_e = \rho_0$: (a) the mass density of pollutants at $t = 1.5\,\mathrm{s}$; (b) the mass density profile at $t = 2.25\,\mathrm{s}$; (c) the velocity vectors

As a consequence of a high value of the emission speed V_{ey}, we observe a generation of vortices (Figure 4b) which make spreading of pollutants more difficult. These vortices propagate essentially horizontally and they are convected a little upwards. This convection occurs as a consequence of the buoyancy force which prevails over the gravitation. The emitted pollution is 5 times warmer than the air and therefore it expands itself at the initial stage of its evolution. This expansion rarefies the pollution (Figure 4c), leading to the occurrence of the buoyancy force.

Figure 5a presents a distribution of pollutants around the smokestack for the density ratio $\rho_e/\rho_0 = 0.75$ at the time $t = 3\,\mathrm{s}$. The velocity vectors at the time $t = 9\,\mathrm{s}$ are shown in Figure 5b. Similarly to the above discussed cases, we see an influence of a resistance of the ambient air. Consequently, the first phase of emission is characterized by spreading of the pollutants in the horizontal direction and generation of two vortices. However, at the height of 7–8 m above the outlet from the smokestack (Figure 5a) a distinct and extended cloud of pollutants is formed. A plume of the pollutants forms below this cloud. At $t = 3\,\mathrm{s}$, the cloud leaves the simulation area. In the simulation area remains, however, the vortex which was formed at the beginning stage of the emission. Initially, this vortex is very static, *i.e.* it does not change its spatial position for $t < 4\,\mathrm{s}$. The buoyancy force that acts on the vortex overcomes the gravity force at the time $t > 4\,\mathrm{s}$ and this vortex moves slowly upward. At the

same time we observe an undisturbed vertical plume of the emitted pollutants (Figure 5b). Such a state of emission cannot, however, be preserved since in the initially motionless air the flow instabilities occur. Consequently, at $t = 9$ s new vortices form at $y = 13\,x_0$ (Figure 5b). Moreover, the energy cascades from larger vortices to smaller vortices which are discernible in Figure 5b at $y \approx 15\,y_0$ and $x = \pm 7\,x_0$. Such a cascade is typical for a turbulent medium (*e.g.* [27]).
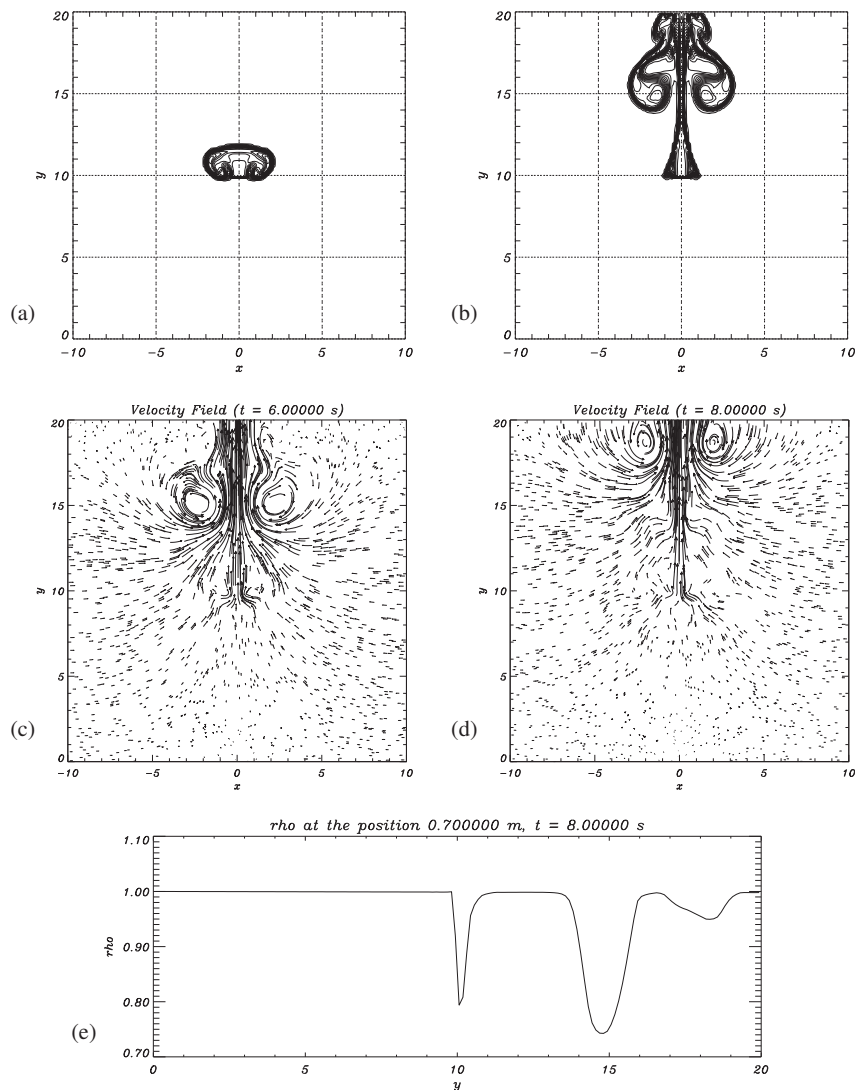

Figure 5. Spatial distribution of pollutants in the case of $\rho_e = 0.75\,\rho_0$: (a) the mass density at $t = 3$ s; (b) the velocity vectors at $t = 9$ s

The velocity vectors of Figure 5b in the neighbourhood of the vertical axis $x = 0$ are directed vertically upwards. Consequently, the pollution movement is not disturbed there. The gas movement at a border between the plume and the ambient air generates the Kelvin-Helmholtz (KH) instabilities which are revealed by vortices. In the case of an incompressible flow a growth rate of the KH instabilities is defined by the following formula:

$$\Im(\omega)^2 = \frac{\rho_0(\rho_0 + \rho_e)}{[\rho_0 + (\rho_0 + \rho_e)]^2}\,[k\,(V_e - V_0)]^2, \tag{79}$$

where ρ_e, ρ_0, V_e and V_0 are the mass densities and speeds of the emitted pollution and the ambient air, respectively $k = \frac{2\pi}{\lambda}$ is the wave number of the wave with its length λ and $\omega = \frac{2\pi}{T}$ is the circular frequency of the wave. The period T corresponds to the appearance of vortices. If we assume that the distance between the neighbouring vortices is equal to the wavelength λ, this period can be estimated as $T \approx 0.6$–0.9 s for $\rho_e/\rho_0 = 0.75$. This period is in agreement with the numerical results.

A scenario of a distribution of light pollutants with $\rho_e/\rho_0 = 0.1$ (Figure 6) resembles the case of the gravitationless atmosphere [23]. At the initial stage of the emission (Figure 6a) a cloud of pollution is generated. A head of this cloud is quite wide due to a resistance of the disturbed ambient air. The spatial scale of these disturbances is much smaller in comparison to the scale in the above discussed cases. As the cloud is rarified, the buoyancy force starts acting upwards. We see this effect in Figure 6b. The cloud is followed by a vertical plume of pollution with speed vectors directed upwards (Figure 6c). Vortices that one can see in Figure 6c at $y = 15\,x_0$ move also upwards (Figure 6d). They influence the plume dynamics as the velocity vectors are deflected from the main direction. This can enhance the plume broadening with the height.

Figure 6. Spatial distribution of pollutants in the case of $\rho_e = 0.1\,\rho_0$: (a) the mass density at $t = 2\,\mathrm{s}$; (b) the mass density at $t = 6\,\mathrm{s}$; (c) the velocity vectors at $t = 6\,\mathrm{s}$; (d) the velocity vectors at $t = 8\,\mathrm{s}$; (e) linear profile of the mass density as a function of the vertical coordinate y for $x = 0.7\,\mathrm{m}$

Figure 6d displays at $y = 14\,x_0$ the air penetrating the plume. This penetration is a consequence of a local decrease of mass density that occurred in the neighbourhood of a plume structure, below a cloud (Figure 6e). As a consequence of that, a tunnel is generated. This tunnel provides an easy way for the air to flow from ambient regions of normal density and pressure ($x > |5|\,\mathrm{m}$, $y \approx 12\,\mathrm{m}$) towards the plume.

The case of the emission with the density ratio $\rho_e/\rho_0 = 0.002$ is shown in Figure 7. The generation of a plume and vortices does not need an additional discussion as the origin of these phenomena is similar to the cases discussed earlier. Figure 7a shows that both the cloud and the plume of pollution are small and they are hardly extended in the horizontal direction. The speed of plume spread is low; it takes 16 s for the plume to reach the height
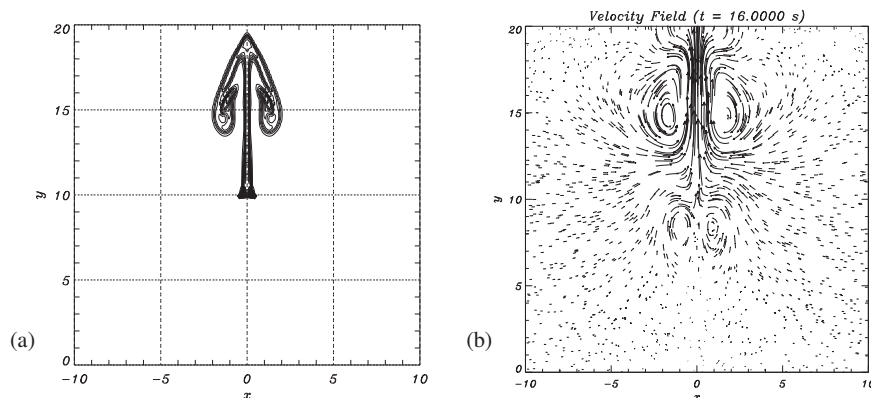
Figure 7. Spatial distribution of pollutants in the case of $\rho_e = 0.002\,\rho_0$: (a) the mass density;
(b) the velocity vectors at $t = 16\,\mathrm{s}$

of 20 m. This amount of time is at least twice as much as we observed in the above discussed cases.

In Figure 7b we see that a vertical flow is driven by vortices. This flow generates a specific way along which pollutants are transported easily upward. The pollution exhibits a small kinetic energy. Therefore, once transported into the height $y = 18\,x_0$ above the vortices (Figure 7b) the pollutants can hardly detach from the whirling cloud to keep moving upward, but their flow is affected by these vortices.

8. Summary

The present paper provides an introduction to modern numerical techniques which can be used for solving dynamics of air-pollutants. With the use of highly efficient present computers it is possible to adapt the latest numerical models which describe physical phenomena by the system of differential equations. The numerical simulations, which have been performed within this study, concern emission and distribution of one-component gas. Our model is of great practical importance and seems to be a valuable tool in a research on propagation of pollutants. This model is expected to provide accurate data for urban and country planning, design of protection zones and location of future emission centers. In the case of numerical simulations, obtaining of the data is faster, cheaper and more precise than in the case of experimental methods being used. As a consequence of that, further studies are highly desirable. In future studies the numerical domain will be enlarged and the wind will be introduced into the model. We hope to observe a developed turbulence which plays a dominant role downwind from the emittor. On the other hand, an incorporation into numerical models boundaries with various permeability properties will make it possible to simulate an influence of buildings and forests on reduction of the expansion of pollutants.

References

[1] LeVeque R J 1997 *CLAWPACK User Notes* Applied Mathematics, Univ. of Washington, Washington, Seattle

[2] Straszko J, Fidecka M and Paulo L A 1997 *Estimation of the quality of the air in the industrial regions* Ochrona powietrza i problemy odpadów **3** 74-82 (in Polish)

[3] Tanaka T and Murawski K 1997 *J. Geophys. Res.* **102** 19805

[4] Yee H C 1989 *A class of high-resolution explicit and implicit shock-capturing methods* NASA Tech. Memo. 101088 and von Karman Institute for Fluid Dynamics Lecture Ser. 1989-04, Rhode-St-Genese, Belgium

[5] De Sterck H and Vanden Abeele D 1997 *EMMA$_D$: a general code for the numerical solution of the equations of MHD on a structured non Cartesian grid* (in preparation)

[6] Godunov S K 1959 *Math. Sb.* **47** 271

[7] van Leer B 1979 *J. Comp. Phys.* **32** 101

[8] Dai W and Woodward P R 1994 *J. Comp. Phys.* **115** 485

[9] Casper J and Atkins 1993 *J. Comp. Phys.* **106** 62

[10] Harten A 1989 *J. Comp. Phys.* **83** 148

[11] Liu X D, Osher S and Chan T 1994 *J. Comp. Phys.* **115** 200

[12] Dai W and Woodward P R 1994 *J. Comp. Phys.* **111** 354

[13] Roe P L 1981 *J. Comp. Phys.* **43** 357

[14] Woodward P R and Colella P 1984 *J. Comp. Phys.* **54** 115

[15] LeVeque R J 1997 *J. Comp. Phys.* **131** 327

[16] Donat R and Marquina A 1996 *J. Comp. Phys.* **125** 42

[17] Einfeld B, Munz C D, Roe P L and Sjögreen B 1991 *J. Comp. Phys.* **92** 273

[18] Harten A and Hyman J M 1983 *J. Comp. Phys.* **50** 235

[19] Murawski K and Goossens M 1994 *Astron. Astrophys.* **286** 943

[20] Stone J M and Norman M L 1992 *I. The hydrodynamic algorithms and tests. Astrophys. J.* **80** 753

[21] LeVeque R J 1996 *Private communication*

[22] Colella P 1990 *J. Comp. Phys.* **87** 171

[23] Michalczyk J K and Murawski K 1999 *Numerical modeling of the continuous emission of the air pollutants* Ochrona powietrza i problemy odpadów **6** 211-218 (in Polish)

[24] Michalczyk J K, Murawski K and Pawłowski L 1999 *Proposals of the numerical simulations of the spreading of pollutants in the ambient air* Ochrona powietrza i problemy odpadów **2** 50-53 (in Polish)

[25] LeVeque R J 1998 *J. Comp. Phys.* **146** 346

[26] Orlanski I 1976 *J. Comp. Phys.* **21** 251

[27] Frisch U 1995 *Turbulence* Cambridge Univ. Press, Cambridge